Biomaterials Science

Milk exosomes anchored with hydrophilic and zwitterionic motifs enhance mucus permeability for applications in oral gene delivery

Journal:	*Biomaterials Science*
Manuscript ID	BM-ART-06-2023-001089.R1
Article Type:	Paper
Date Submitted by the Author:	29-Sep-2023

Complete List of Authors:	Zhang, Chenzhen; Northeastern University - Boston Campus, Department of Bioengineering Zhang, Hengli; Northeastern University - Boston Campus, Department of Bioengineering Millán Cotto, Héctor; Northeastern University - Boston Campus, Department of Bioengineering Boyer, Timothy; Northeastern University - Boston Campus, Department of Bioengineering Warren, Matthew; Northeastern University - Boston Campus, Department of Bioengineering Wang, Chia-Ming; Northeastern University - Boston Campus, Department of Bioengineering Luchan, Joshua; Northeastern University - Boston Campus, Department of Bioengineering Dhal, Pradeep; Sanofi SA, R&D Carrier, Rebecca; Northeastern University - Boston Campus, Department of Chemical Engineering Bajpayee, Ambika; Northeastern University - Boston Campus, Department of Bioengineering

Milk exosomes anchored with hydrophilic and zwitterionic motifs enhance mucus permeability for applications in oral gene delivery

Received 00th January 20xx,
Accepted 00th January 20xx

DOI: 10.1039/x0xx00000x

Chenzhen Zhang, †[a] Hengli Zhang, †[a] Héctor A. Millan-Cotto,[a] Timothy L. Boyer,[a] Matthew R. Warren,[a] Chia-Ming Wang,[a] Joshua Luchan,[a] Pradeep K. Dhal,[b] Rebecca L. Carrier,[c] and Ambika G. Bajpayee[a]

Exosomes have emerged as a promising tool for the delivery of drugs and genetic materials, owing to their biocompatibility and non-immunogenic nature. However, challenges persist in achieving successful oral delivery due to their susceptibility to degradation in the harsh gastrointestinal (GI) environment and impeded transport across the mucus-epithelium barrier. To overcome these challenges, we have developed high-purity bovine milk exosomes (mExo) as a scalable and efficient oral drug delivery system, which can be customized by incorporating hydrophilic and zwitterionic motifs on their surface. In our study, we observed significantly improved transport rates by 2.5-4.5x in native porcine intestinal mucus after the introduction of hydrophilic and zwitterionic surface modifications, as demonstrated by tranwell setup and fluorescence recovery after photobleaching (FRAP) analysis. Remarkably, mExo functionalized by a block peptide (BP), consisting of cationic and anionic amino acids arranged in blocks at the two ends, demonstrated superior tolerability in the acidic gastric environment (with a protein recovery rate of 84.8 ± 7.7%) and exhibited a 2.5-fold increase in uptake by intestinal epithelial cells. Furthermore, both mExo and mExo-BP demonstrated successful intracellular delivery of functional siRNA, resulting in up to 65% suppression of the target green fluorescence protein (GFP) gene expression at a low dose of siRNA (5 pmol) without causing significant toxicity. These findings highlight the immense potential of modifying mExo with hydrophilic and zwitterionic motifs for effective oral delivery of siRNA therapies.

1. Introduction

Oral administration is the preferred route for biological therapeutics due to its simplicity, convenience, and high patient compliance. However, the gastrointestinal (GI) mucus-epithelial barrier poses a significant obstacle to permeation of orally introduced drugs into the bloodstream. This physical protective system sterically hinders the transport of micro-organisms and noxious molecules. It can also impede the transport of therapeutics, significant reducing their overall bioavailability [1-4]. Moreover, orally delivered drugs face a wide range of pH conditions traveling from the acidic gastric environment to the neutral intestinal tract, which combined with the presence of various digestive enzymes, can limit drug bioactivity [5-10]. Thus, there is a pressing need to develop engineered nanocarriers for efficient oral delivery. Recent studies have utilized exosomes, known for their biocompatible intercellular communication and cargo delivery properties, to deliver peptides, nucleic acid, and small molecules [11]. Compared to liposomes and polymeric nanoparticles, exosomes are advantageous due to their innate reduced toxicity and ability to avoid immune clearance [12]. However, like other molecules, exosomes face degradation in the GI environment and hindered permeation through the mucus-epithelial barrier [6]. Thus, orally delivered exosomes must be further engineered to improve their therapeutic efficacy.

An effective mucus penetrating nanocarrier requires several design considerations. Hydrophobic surfaces of nanocarriers may be undesirably trapped in the mucus layer via interactions with hydrophobic domains of mucin [7, 13]. Moreover, particles with a near-neutral zeta potential (ζ) exhibit the most efficient diffusion through mucus [14]. Therefore, current mucus penetration strategies focus on neutralizing the surface charge and shielding the hydrophobic surface properties of nanocarriers. In our previous work, we surface coated bovine milk derived exosomes (mExo) with polyethylene glycol (PEG), providing a hydrophilic coating to reduce interactions between mExo particles and mucus. The PEGylation of mExo enhanced intestinal mucus penetration and improved stability, while allowing effective intracellular siRNA delivery [6]. However, PEGylated mExo suffered from about 50% loss of protein content when exposed to the acidic GI environment, and exhibited limited epithelial cell communication and uptake due to its hydrophilic coating [6]. Compared to cell-derived exosomes, mExos were chosen as they exhibit enhanced yield with low costs, while still demonstrating effective nucleic acid delivery [15-18].

Several alternative approaches have been proposed to enhance mucus penetration. Leal *et al*. modified phages with peptides that mimic the repeat 'PTS domain' (proline, threonine, and serine) sequences in mucin monomer, reducing intermolecular interactions with mucus [19]. As a result, phages with mucin-mimicking peptide (ISLPSPT) showed 2.6-fold greater diffusion compared to unmodified phages [19]. However, while these hydrophilic surface coating strategies enhance mucus penetration, they have the potential to hinder carrier-to-cell interaction that occur when particles reach the epithelial layer [20]. An alternative strategy that allows transport through both the mucus and the epithelial barrier is to design particle surfaces those mimic viruses with dense, net neutral zwitterionic surface [5, 21]. Zwitterionic nanocarriers exhibit favorable hydrophilicity and reduced non-specific protein adsorption. Dilauroylphosphatidylcholine (DLPC) surface-

[a] *Departments of Bioengineering, Northeastern University, Boston, MA, 02115, USA.*
[b] *Sanofi SA Global R&D, Waltham, MA, 02451, USA.*
[c] *Department of Chemical Engineering, Northeastern University, Boston, MA, 02115, USA*
† These authors contributed equally to this work.
Electronic Supplementary Information (ESI) available: [details of any supplementary information available should be included here]. See DOI: 10.1039/x0xx00000x

modified polylactic acid (PLA)-based zwitterionic nanoparticles were developed recently that exhibited a 6.3-fold higher diffusivity through mucus compared to polyvinyl alcohol (PVA) nanoparticles and improved the oral bioavailability of insulin by 6.9-fold [22]. Additionally, the spatial distribution between charged motifs on zwitterionic molecules may further affect mucus transport properties [22]. For instance, using a mucus based microfluidic model, transport of zwitterionic peptides comprising of alternating (AP) or blocked (BP) lysine and glutamic acid residues was studied [23]. In the case of BP, the term 'block' denotes that the lysine and glutamic acid residues are grouped at two distinct ends $(AE)_5(AK)_5$ whereas AP has the alternating structure $(AEAK)_5$. While AP showed no significant interaction with mucin, BP accumulated at the mucus surface, suggesting the cationic block exhibits unique transport behaviour [23].

Table1. Amino acid sequence, molecular weight, and net charge at pH 7 of peptides

Peptides	Sequence	Molecular weight	Net charge at pH 7
Mucin-mimicking peptide	ISLPSPT	714 Da	0
Alternating peptide	$(AEAK)_5$	2015 Da	0
Block peptide	$(AE)_5(AK)_5$	2015 Da	0

In this study, we developed three strategies for mExo surface modification to accelerate their penetration through the GI mucus-epithelium barrier (see **Fig. 1** and **Table 1**). First, PEGylation was introduced to increase the hydrophilicity of mExo and prevent hydrophobic interactions. As a second strategy, a mucin-mimicking peptide (MP) with a sequence similar to the hydrophilic PTS domain of mucin monomers was introduced. Thirdly, AP, BP, and DLPC zwitterionic motifs were anchored on the mExo surface to imitate mucus-penetrating viruses. For BP, the cationic charge block was placed at the outer peptide terminus (mExo-linker-N-AE_5-AK_5-C), which we hypothesized would enhance mExo-cell communication and uptake (**Fig. 1**). Additionally, we computationally predict BP may exhibit enhanced secondary structure compared to AP, which may explain its improved mExo stability in the harsh GI environment and increased cellular uptake. Finally, we demonstrated that siRNA-loaded, surface-modified mExo can functionally deliver siRNA and silence a target gene *in vitro*, making them a promising naturally derived cell-free nanocarrier for oral delivery of siRNA.

2. Methods

2.1 Materials

Fat-free bovine milk (HP Hood, Lynnfield, MA) was purchased from a local supermarket. The peptides (**Table 1**) were synthesized from MIT Biopolymers and Proteomics (Cambridge, MA). 2-Dilauroyl-sn-glycero-3-phosphocholine (DLPC) was bought from Echelon Biosciences (Salt Lake City, UT). 1,2-distearoyl-sn-glycero-3-phosphoethanolamine-N [azido (polyethylene glycol)-2000] [6, 17] (DSPE-PEG-Azide) was purchased from Avanti Polar Lipids (Alabaster, AL). qEV10 35 nm SEC column was purchased from Izon Science (Medford, MA). GFP-expressing HEK293 cells were purchased from Cell Biolabs (San Diego, CA). The corresponding GFP silence siRNA – GFP Duplex I was purchased from Dharmacon (Lafayette, CO). Native porcine intestinal mucus was harvested from Research 87 Inc. Trypsin-EDTA, 4',6-Diamidino-2-Phenylindole, Dihydrochloride (DAPI), Pepsin, Trypsin, Lipase, Bile Salt, phosphatidylcholine (PC), Lipofectamine 2000 reagent, micro-bicinchoninic acid (BCA) assay kit, and miRNA Isolation Kit were purchased from Thermo Fisher (Waltham, MA). Lipopolysaccharide (LPS), 100 kDa molecular weight cut-off (MWCO) Amicon Ultra Centrifugal Filters, N,N-Dimethylformamide (DMF), and Fluorescein isothiocyanate (FITC) isomer I were bought from Sigma-Aldrich (St. Louis, MO). Cyanine5 (Cy5) NHS ester and Dibenzocyclooctyne-N-hydroxysuccinimidyl (DBCO-NHS) ester were purchased from Lumiprobe (Cockeysville, MD). Ethylenediaminetetraacetic acid (EDTA) was bought from Quality Biological (Gaithersburg, MD). Paraformaldehyde (PFA), Triethylamine (TEA), Dimethyl Sulfoxide (DMSO), and all salts from simulation digestion electrolyte (**Table 2**) were purchased from Fisher BioReagents (Pittsburgh, PA). Cell culture related reagents: Phosphate Buffered Saline (PBS), High-glucose Dulbecco's Modified Eagle Medium (DMEM), Fetal Bovine Serum (FBS), GlutaMAX, non-essential amino acids (NEAA), penicillin-streptomycin antibiotic-antimycotic (PSA), Roswell Park Memorial Institute (RPMI) 1640, and Opti-MEM were purchased from Gibco (Grand Island, NY). Heat-inactivated fetal bovine serum (HI-FBS) was purchased from R&D Systems (Minneapolis, MN). Fluorochrome-conjugated anti-human antibodies: CD86 (PE-Cy5), CD197 (AlexaFluor488), CD80 (PE-Cy7), CD163 (Brilliant Violet 510), Macrophage colony-stimulating factor (M-CSF), and granulocyte macrophage colony-stimulating factor (GM-CSF) were purchased from Biolegend (San Diego, CA). Exoquick-TC, ExoGlow, and CD63 Exo-Flow Capture Kit were purchased from

Table 2. The composition of simulated digestive electrolyte solution. Final pH was adjusted with 1N HCl to correspond with each simulated digestive pH, then filled with DI water for a total of 20 mL.

Electrolyte	Stock Molarity (M)	SSF (µL)	SGF (µL)	SIF (µL)
KCl	0.50	528.50	258.75	187.00
KH_2PO_4	0.50	129.50	33.75	22.00
$NaHCO_3$	1.00	238.00	270.00	144.65
NaCl	2.00	0.00	442.50	264.00
$MgCl_2(H_2O)_6$	0.15	17.50	15.00	30.25
$(NH4)_2CO_3$	0.50	2.10	18.75	0.00
$CaCl_2$	0.30	100.00	10.00	40.00
HCl	6.00	31.97	57.92	19.25

System Bioscience (Palo Alto, CA). PureLink miRNA Isolation Kit was purchased from Invitrogen (Waltham, MA).

2.2 Milk exosome (mExo) harvest

The methodology used to harvest and purify milk exosomes has previously been described in detail by our group [6]. Briefly, we mixed 108 mL of bovine milk with 180 mL of PBS and centrifuged it at 3000 g for 15 minutes to pellet cells and cellular debris. We collected 102 mL of milk supernatant below the liquid surface layer, discarding the floating fat. An equal volume of 0.25 M EDTA was added to the collected supernatant and placed in an ice bath for 15 minutes to chelate casein-calcium complexes. The mixture was then ultra-centrifugated (Sorvall WX100, Thermo Fisher, Waltham, MA) in four steps (12,000 g, 35,000 g, and 70,000 g for 1 hour each, and 100,000 g for 2 hours) to create and collect mExo pellets. Finally, we used a qEV10 35 nm SEC column to further purify the pooled mExos.

2.3 Conjugation of peptides to DSPE-PEG-azide

Sequence, molecular weight, and net charge at pH 7 of peptides are shown in **Table 1**. DBCO-NHS ester was used to link DSPE-PEG-azide lipid to peptides. Five equivalents of DBCO-NHS ester (0.28 mg) and one equivalent of peptides were dissolved in 0.6 mL of anhydrous DMF. TEA was used to adjust the DMF pH to be between 7 and 8 for site-specific conjugation at the N-terminus of peptides. The vial was purged full of nitrogen gas and the reaction was stirred at room temperature overnight. The synthesized DBCO-peptide products were dialyzed in a 1 kDa MWCO dialysis tube against PBS for 3 days to remove impurities. After purification, the products were lyophilized (~30% recovery) and dissolved in DMSO to make a concentration of 5 mg/mL. DBCO-peptide DMSO solution reacted with 1.2 equivalents of DSPE-PEG-azide dissolved in DMSO (5 mg/mL) at room temperature overnight. The final product, DSPE-PEG-peptides, were added dropwise into PBS to make a DSPE-PEG concentration of 25 μg/mL for subsequent experiments.

2.4 mExo surface modification

The DSPE-PEG-peptides were anchored on the surface of the mExo by adding 165 μg of mExos to 1 mL of the prepared DSPE-PEG-peptides solution and stirred for 1 hour at 37 °C. The mExo to DSPE-PEG-peptides molar ratio was 1:10,000, resulting in approximately 500 DSPE-PEG-peptide molecules per mExo. The excess DSPE-PEG-peptides were purified from the solution using a 100 kDa MWCO centrifugal filter. The method of DLPC insertion was the same as that of DSPE-PEG-peptides. Briefly, one equivalent of mExo was mixed with 10,000 equivalents of DLPC at 37 °C for 1 hour, followed by purification using a 100 kDa MWCO centrifugal filter.

2.5 mExo characterization

The size and zeta potential of mExos were measured using a Particle Analyzer (Litesizer 500, Anton Paar, Graz Austria) and were confirmed by transmission electron microscopy (TEM, JEM-1010, JEOL USA, Peabody, MA) using the negative staining method. The fluorescence intensities of fluorescence-labeled lipids, peptides, and mExos were measured with a Synergy H1 plate reader (BioTek, Winooski, VT), and converted to concentrations using the corresponding standard curves, to obtain the loading molar ratio of lipids or peptides to mExos. DSPE-PEG and DSPE-PEG-peptide insertion was verified using the CD63 Exo-Flow Capture Kit (System Bioscience, Palo Alto, CA) for flow cytometry. Following the kit manual, 40 μL of 9.1 μm streptavidin magnetic beads were washed with bead wash buffer. The magnetic beads were immobilized at the bottom of an Eppendorf tube using magnetic adsorption, and the supernatant was discarded. The magnetic bead pellets were incubated with 10 μL of CD63 antibody solution on ice for 2 hours, gently mixing every 30 minutes, to coat the bead surface with anti-CD63. These beads were then resuspended in 400 μL of wash buffer and prepared for mExo-beads binding. mExo surface proteins were labelled with FITC while PEG and BP were labelled with Cy5. 100 μL of native or surface-modified mExo samples were added to 400 μL of prepared anti-CD63 coated bead solution and incubated overnight at 4°C. After washing out uncaptured mExo, the fluorescence labels on the beads were analysed using a Cytoflex flow cytometer (Beckman Coulter, Brea, CA) with FITC-A and APC-A channels. Forward scatter area (FSC-A) and side scatter area (SSC-A) were co-analysed to select single beads.

2.6 Stability of surface modified mExo in simulated gastrointestinal (GI) conditions

The enzyme-deficient simulated digestive electrolyte solutions used here mimic the three primary GI environments orally-administered mExos would encounter. These include simulated salivary fluid (SSF) in the oral phase (pH 7), simulated gastric fluid (SGF) in the gastric phase (pH 2.2), and simulated intestinal fluid (SIF) in the intestinal phase (pH 7). All simulated digestive electrolyte solutions were prepared with the chemical compositions detailed in **Table 2**. To prepare enzyme-rich SGF, 900 unit/mL of pepsin and 37.5 unit/mL of lipase were added to the enzyme-deficient SGF electrolyte. For enzyme-rich SIF, 36 μg/mL of trypsin and synthesized bile containing phosphatidylcholine (PC) and bile salt at 10 mM were added to the enzyme-deficient SIF electrolyte [24, 25]. The pH of the solutions was adjusted using 1N HCl and 1N NaOH and filled to a 20 mL volume with DI water. Native and surface-modified mExos (75 μg) were gently stirred within 1 mL of each simulated digestive electrolyte solution at 37 °C, respectively. mExos were extracted at designated times (SSF at 5 min, SGF at 2 hours, SIF at 2 hours). The low pH environment of the gastric fluid may cause degradation of mExos leading to loss of their protein content. Following exposure to simulated GI fluids, intact mExos were collected using a 100 kDa MWCO centrifugal filter and then analysed using the BCA kit to obtain the remaining protein content. The recovery was calculated by dividing the remaining protein content by the original amount measured in the PBS environment. The size of the mExos after exposure to the simulated GI fluids was characterized using the Particle

Analyzer. The morphology of these mExos was further analysed by transmission electron microscopy (TEM, JEM-1010, JEOL USA, Peabody, MA) using the negative staining method.

2.7 Intestinal mucus transport

The mucus transport properties of native and surface-modified mExos were investigated using an *in vitro* transwell setup. As shown in **Fig. 3A**, 40 µL of native porcine intestinal mucus was added to the 0.4 µm polycarbonate membrane transwell inserts (0.33 cm^2 surface area), forming a ~0.2 mm thick mucus layer. The acceptor chamber of the transwell was filled with 600 µL of PBS. On the surface of the mucus layer, 15 µL of ExoGlow Green-labelled native or surface-modified mExos were added, respectively. The well plate was immediately covered and moved to 37 °C with light shaking for the designated amount of time (5, 10, 20, 30, 45, and 60 min). Finally, the PBS from the acceptor chamber was collected for mExo fluorescence measurement using the Synergy H1 plate reader. The fluorescence of the original mExo solution was also measured before adding it to the donor chamber. In parallel, 15 µL of 30 µM FITC was added to the mucus layer in the donor chamber as a control group. The apparent permeability coefficient (P_{app}) was calculated by the following formula:

$$P^{app} = \frac{dRFU}{dt} * \frac{1}{A * RFU_0}$$

where *RFU* is the fluorescence intensity of collected PBS from acceptor chamber, RFU_0 is the starting solution fluorescence, and *A* is the surface area of the transwell insert membrane.

2.8 Fluorescence recovery after photobleaching (FRAP) analysis

Fluorescent recovery after photobleaching (FRAP) involves irreversible photobleaching in a small region of interest and then tracking of the recovery of fluorescence intensity in that region as fluorescent particles from the surrounding area diffuse in to replace those that have been photobleached [26, 27]. The resulting curve is used to estimate the effective diffusion coefficient (D_{eff}) and mobile fraction (K) of the particles, indicative of the level of hinderance the particles encounter in the system [26, 27]. In this study, FRAP measurements were made using a ZEISS LSM 880 inverted confocal microscope (Carl Zeiss NTS Ltd., Oberkochen, Germany) equipped with a 40x water immersion magnification objective. Four-chamber slides were used to hold 400 µL aliquots of carefully homogenized mucin samples for each particle condition. FITC-labeled mExo particles (20 µL) were superficially injected into the center of the well using a pipette and then incubated for 30 minutes in a sealed, humid, and dark environment to prevent evaporation and accidental photobleaching.

Once incubation was complete, FRAP experiments were performed. Regions of interest were 28 µm in diameter and measurements were repeated throughout the length of the well to minimize regional bias. The D_{eff} was obtained from fitting the fluorescence recovery curve to:

$$f = \sum_{n=1}^{\infty} \frac{(-\kappa)^n}{n!} \cdot \frac{1}{1 + n\left[1 + 2\frac{t}{\tau}\right]} \quad (1)$$

where t is the time in seconds, τ is the characteristic diffusion time, and κ represents the depth of bleaching calculated as:

$$\frac{(1 - e^{-\kappa})}{\kappa} = \frac{F_i}{F_0} \quad (2)$$

where F_i is the initial fluorescence of the region of interest and F_0 is the fluorescence right after photobleaching. The mobile fraction, *K* was calculated as follows:

$$K = \frac{F(t) - F_0}{F_i - F_0} \quad (3)$$

where *F(t)* is the fluorescent recovery curve of the region of interest over time. The τ was defined as the time it takes for the curve to reach 50% of its maximum intensity and is related to the D_{eff} as follows:

$$D_{eff} = \frac{\omega^2}{4\tau} \quad (4)$$

where ω is a measure of the width of the laser's Gaussian beam (e^{-2} halfwidth).

Lastly, to better understand how particle population would travel through the entirety of the mucus, we calculated an approximate of the population's flux, average diffusion (P_A). FRAP separates the particle flux into the diffusion and fraction of the mobile particles which ignores immobilized ones. Therefore, P_A offers an estimation of the entire population's flux through mucus by averaging the diffusion of both mobile and immobile particles. The P_A was calculated as:

$$P_A = K * D_{eff} \quad (5)$$

2.9 *In vitro* cellular uptake, cytotoxicity, and immunogenic response analysis

The human epithelial cell line Caco-2 was used as a model for intestinal epithelial uptake and cytotoxicity studies. Caco-2 cells were seeded in a 96-well plate at a concentration of 10,000 cells/well using complete culture media containing high-glucose DMEM, 10% FBS, 1% GlutaMAX, 1% non-essential amino acids (NEAA), and 1% penicillin-streptomycin antibiotic-antimycotic (PSA) and incubated for 16 hours. Then, 200 µL of complete culture media containing 50 µg of ExoGlow Red labeled native and surface-modified exosomes were added to each well (N = 6/group), respectively, and incubated for 2.5 hours at 37°C in a 5% CO_2 environment. After uptake, the treated Caco-2 cells were washed with cold PBS and stained with DAPI. The colocalization of exosomes and Caco-2 cells was observed under the fluorescence microscope at 350/470 nm excitation/emission wavelength and 573/588 nm excitation/emission wavelength. For flow cytometry analysis

(using CytoFLEX, Beckman Coulter, CA), Caco-2 cells were detached using 0.25% trypsin-EDTA, washed with cold PBS at least three times, and then resuspended in 600 µL of PBS. The FITC signal in the treated cells was acquired, and at least 10,000 cells were analysed for each sample. For cytotoxicity analysis, Caco-2 cells were cultured with 100 µL of 1.2 mM 3-(4,5-dimethylthiazol-2-yl)-2,5-diphenyltetrazolium bromide (MTT) solution for 4 h at 37°C. After culture, 25 µL of media from each well of Caco-2 cells was mixed with 50 µL of DMSO for 10 minutes. The absorbance of MTT assay was measured at 540 nm wavelength. The immunogenicity response of mExo and mExo-BP was evaluated by determining their interactions with human monocyte-derived macrophages using flow cytometry, focusing on the expression of M1 pro-inflammatory and M2 anti-inflammatory polarization markers [28-30]. Human monocytes isolated from peripheral blood were seeded in 6-well plates at a density of 880,000 cells/well. Over a span of 7 days, differentiation into macrophages was facilitated using a medium comprising RPMI 1640, 10% HI-FBS, 1% GlutaMax, 1% PSA, and 100 ng/mL M-CSF [28]. Following differentiation, macrophages were collected, resuspended in complete cell culture media — which contained high-glucose DMEM, 10% HI-FBS, 1% GlutaMAX, 1% NEAA, and 1% PSA — and subsequently seeded in 24-well plates at a density of 40,000 cells/well. For M1-polarization positive control group, an addition of 50 ng/mL GM-CSF and 10 ng/mL LPS was included. Both mExo and mExo-BP were introduced at a particle concentration of 1,000 particles/cell. After incubating for an additional 48 hours, cells were harvested. These were then labeled with a cocktail of antibodies, consisting of 0.2 µL each of CD86 (PE-Cy5), CD197 (AlexaFluor488), CD80 (PE-Cy7), and CD163 (Brilliant Violet 510). This labelling process lasted for 30 minutes, after which cells were fixed with 4% PFA for another 30 minutes. The CytoFLEX system (Beckman Coulter, CA) was used to perform flow cytometric analyses, capturing signals from each antibody to delineate the expression levels of specific cell surface markers.

2.10 Molecular Dynamics (MD) simulation of peptides

Peptides were folded with AlphaFold [31, 32] and were prepared using Schrödinger suite 2022-2 (D.E. Shaw Research, New York City, NY) using the protein preparation workflow. Hydrogens and terminal oxygens were added and optimized at pH 7.0 or 2.2. N termini were capped with an extra acetyl group. Peptides were then solvated in an orthorhombic TIP3P water box with 0.15M NaCl with at least 20 Å between boundary and closest peptide edge on all sides. All simulations used the OPLS4 force field [33]. Each peptide was relaxed by the default Desmond minimization steps. Peptides were simulated for 100 ns at NPT, 310.15 K, 1.013 bar, and a frame was recorded every 20ps. Smooth particle mesh Ewald method was used for efficient evaluation of long-range electrostatics. The Martyna-Tuckerman-Klein [34] and Nosé-Hoover [35] chain coupling schemes were used to control pressure and temperature at relaxation times of 1.0 and 2.0, respectively. Simulations were run on NVIDIA Tesla v100-sxm2 with Research Computing at Northeastern University. The Root Mean Square Deviation (RMSD), Root Mean Square Fluctuation (RMSF), and secondary structure prediction were calculated from each trajectory using Schrödinger's built-in Simulation Interactions Diagram.

2.11 mExo-siRNA loading and HEK293 silencing

A chemical exosome transfection reagent, Lipofectamine 2000 (Lipo), was used to load siRNA into mExo. Initially, 4 µL of siRNA (20 pmol/µL) and 5 µL of Lipo stock (1mg/mL) were diluted each in a 40 µL Opti-MEM solvent for the following experiments. These two solutions were mixed in a 1:1 v/v ratio and incubated at room temperature for 10 min. The resulting 80 µL Lipo-siRNA complex was then mixed with 75 µg of native or surface-modified mExo and gently shaken for 30 minutes at room temperature. The siRNA-loaded mExo was pelleted at 15,000 g for 5 min with the addition of Exoquick-TC. The supernatant was discarded, and the pellets were washed with PBS and resuspended in 100 µL Opti-MEM. To calculate the siRNA loading efficiency, siRNA was first isolated from its loaded mExo using the small RNA Isolation Kit by following the one-column protocol provided in the user manual from PureLink. The siRNA content was then measured using the Qubit 4 Fluorometer (ThermoFisher Scientific, Waltham, MA). The loading efficiency was calculated by dividing the amount of loaded siRNA by the initial amount of siRNA added to the mExo during the loading process.

GFP-expressing HEK293 cells were used as a model for *in vitro* gene silencing experiments. The cells were seeded in a 48-well plate at a concentration of 25,000 cells/well using antibiotic-free culture media containing high-glucose DMEM, 10% FBS, 1% GlutaMAX, and 1% NEAA. After 24 hours of culture at 37 °C in a 5% CO_2 environment, the cells reached up to 80% confluence. Then, mExo and surface-modified mExo (12.5 and 50 µg) loaded with 5 pmol and 20 pmol of siRNA were added to each well plate (N = 6/group), respectively. The same dose of siRNA was mixed with Lipo at a 1:1 v/v ratio as a positive control. The media was changed to complete culture media containing 1% PSA, and the cells were cultured at 37 °C in a 5% CO_2 environment for 4 h. After 3 days of incubation, the cells were imaged under the Bright-Field and FITC channels of a fluorescence microscope to monitor GFP silencing. The treated HEK293 cells were then detached by 100 µL of 0.25% Trypsin-EDTA and washed with PBS for flow cytometry analysis. The GFP fluorescence intensity of the HEK293 cells was quantified using the Beckman Coulter Cytoflex flow cytometer under FITC-A channel, with 10,000 cells counted for each analysis.

2.12 Statistical analysis

All data are presented as mean values ± standard deviation. N = 4 - 6 formulation repeats were used for characterization and stability studies in **Fig. 2**. In mucus transport studies, N = 3 – 6 repeats of each group were used for data presented in **Fig. 3**. For cell culture experiments, N = 6 repeats per condition were used in **Figs. 4 and 6**. One-way analysis of variance (ANOVA) and post-hoc Tukey's honestly significant difference (Tukey's HSD)

test was used for comparisons between experimental groups. p values less than 0.05 were considered statistically significant.

3. RESULTS

3.1 mExo harvest and surface modification

Table 3. Diameter size (nm), zeta potential ξ (mV), polydispersity index (PDI) and loading of lipid insertions on mExo membrane

	mExo	mExo-PEG	mExo-DLPC	mExo-MP	mExo-AP	mExo-BP
Size (nm)	168.7 ± 17.6	170.8 ± 4.4	173.2 ± 7.7	206.59 ± 14.4	179.4 ± 8.1	189.4 ± 10.0
ξ (mV)	-25.4 ± 1.3	-16.6 ± 0.8	-11.2 ± 1.6	-23.4 ± 1.6	-15.9 ± 1.7	-16.6 ± 1.4
Loading (per Exo)	N/A	505	N/A	319	314	367
PDI	0.199	0.136	0.197	0.212	0.184	0.252

The eluted SEC fractions 5 - 7 from mExo purification were expected to result in the desired mExo size range of 40 - 200 nm diameter with a high purity in the range of 3.0 ± 0.6 x 10^9 particles per μg protein based on our prior work [6]. The highest protein concentration was in fraction 6 at 654.3 ± 32.4 μg/mL, measured by BCA assay (**Fig. 2A**). Therefore, fractions 5 - 7 were collected for surface modification and further studies. As shown in **Table 3**, the surface modifications slightly increased the hydrodynamic diameter of mExos but with no statistically significant difference compared to unmodified mExo. Further, the zeta potential (ξ) of mExos was partially shielded by the coating of lipids and peptides. Approximately 300-500 moles of lipids and peptides were calculated to be anchored on each mExo membrane (**Table 3**). TEM images confirmed the consistent size and saucer-like morphology for both native and surface-modified mExos (**Fig. 2B**). Flow cytometry analysis was performed on dual-labeled mExo-PEG and mExo-BP samples, where mExo was labeled with FITC and peptides with Cy5 (**Fig. 2C**). The magnetic beads with CD63 antibody effectively captured mExo, as evidenced by the high FITC intensity observed. The high Cy5 intensities under the APC channel for both mExo-PEG and mExo-BP samples confirmed the successful surface modification of mExo. Additionally, flow analysis demonstrates that lipid insertion did not interfere with the binding between CD63 proteins expressed on the mExo membrane and the CD63 antibody, indicated by the similar FITC fluorescence intensities of mExos binding to beads before or after PEGylation. These findings indicate that the surface modification of mExo with specific peptides will not interfere with the binding and reorganization of exosome surface proteins by cells for biological communication.

3.2 *In vitro* stability of native and surface-modified mExos in simulated gastrointestinal (GI) conditions

This study assessed the stability of native and surface-modified mExo in GI environments by evaluating their size variation and protein loss under enzyme-deficient and enzyme-rich simulated digestion conditions. The simulated saliva fluid (SSF, pH 7), gastric fluid (SGF, pH 2.2), and intestinal fluid (SIF, pH 7) represent the three phases of intestinal transit. All formulations were found to have no significant change in size following their incubation in enzyme-deficient gastric fluids (**Fig. 2D**). Native and surface-modified mExos were found to be stable following their treatment with SSF based on protein recovery measurements (**Fig. 2D**), as expected. While mExo-DLPC exhibited similar protein loss compared to native mExo (15.4 ± 1.1%), the other surface-modified mExo with hydrophilic PEG coatings showed superior protein recovery in SGF. TEM images revealed that native mExos lost their original morphology, further confirming their digestion in enzyme-deficient SGF (**Fig. S1**)**.** mExo-BP remained most stable with the highest protein recovery in both SGF (84.8 ± 7.7%) and SIF (95.7 ± 7.7%), even outperforming mExo-AP, which has a similar residue composition but different spatial charge distribution. However, when formulations were incubated in enzyme-rich SGF, a significant drop in mExo stability was observed as the protein recovery in all formulations reduced to about 10-30% of the pre-incubation amount (**Fig. S2**)**.** Following incubation in SIF supplemented with trypsin and synthetic bile, protein recovery for all formulations reduced to 40-70% of the pre-incubation amount compared to that measured in the presence of enzyme-deficient SIF (over 80%, **Fig. 2D**). Addition of surface motifs helped improve stability of mExo formulations in the presence of enzymes. The relatively lower protein recovery observed in SGF underscores the need for additional enteric coatings on mExo surface to augment its delivery efficacy and pharmaceutical application [9].

3.3 *In vitro* porcine mucus transport study

We evaluated the mucus transport properties of these surface-modified mExos in porcine intestinal mucus using the transwell chamber setup shown in **Fig. 3A**. FITC was selected as the negative control representing a small molecule drug. The measured apparent permeability coefficient (P_{app}) of FITC was

>10 times lower than that of native mExo. PEGylation of mExo increased the P_{app} by ~2 times due to the improved hydrophilicity of mExo and weakened hydrophobic interactions with mucus, which is consistent with our previous work [6]. By introducing the zwitterionic and mucin-mimicking peptides, the interactions between mucus and surface-modified mExos were further reduced, resulting in 2.5 to 4.5 times faster transport rates through the mucus layer (**Fig. 3B**). There is no significant difference between these zwitterionic, and mucin-mimicking peptides modified mExo.

Table 4. The calculated 50% fluorescent recovery ($\tau_{1/2}$), mobile fraction (K), diffusion coefficients (D_{eff}), and average diffusion (P_A) were obtained from FRAP experiments. Values are presented as mean ± standard deviation.

	mExo	mExo-PEG	mExo-MP	mExo- DLPC	mExo-AP	mExo-BP
K	0.25 ± 0.02	1.05 ± 0.05	0.70 ±0.1	0.90 ± 0.27	0.78 ± 0.07	0.86 ± 0.1
$\tau_{1/2}$ [s]	24.9 ± 2.0	24.2 ± 4.3	24.1 ± 9.2	33.5 ± 6.0	21.6 ± 3.8	40.9 ± 3.5
D_{eff} [x10^{-2}µm^2/s]	3.40 ± 0.28	3.35 ± 0.73	3.96 ± 1.2	2.59 ± 0.45	4.01 ± 0.66	2.33 ± 0.54
P_A [x10^{-2}µm^2/s]	0.86 ± 0.07	3.35 ± 0.73	2.79 ± 0.87	2.33 ± 0.41	3.11 ± 0.52	2.11 ± 0.40

3.4 Fluorescent recovery after photobleaching (FRAP) analysis

Surface-modified mExo demonstrated enhanced mucus mobility in FRAP experiments. The mobile fraction of all surface-modified mExo significantly improved over that of unmodified mExo, with mExo-PEG demonstrating full mobility (*K,* mExo vs mExo-PEG: 25 ± 2%, 100 ± 5%) (**Fig. 3D, Table 4**). No significant difference was observed between surface-modified mExos. However, it was noted that the mExo demonstrated a D_{eff} similar to mExo-PEG (**Table 4**). It is hypothesized that the fraction of immobilized mExo particles is substantial enough to saturate all hydrophobic interactions in the region of interest, thereby permitting the remaining mobile fraction to diffuse unimpeded. Consequently, due to their similar sizes, the D_{eff} between native and surface-modified mExo formulations is statistically indistinguishable. Incorporating the average diffusion P_A, which represents the flux of the entire population, presents a trend that aligns more closely with what was observed in the *in vitro* transwell study. Surface-modified mExo particles recorded a higher P_A, suggesting significantly faster diffusion compared to unmodified exosomes, due to the shielding of hydrophobic interactions with the hydrophobic domain in mucin (**Fig. 3D**). Interestingly, mExo-BP particles exhibited a relatively lower P_A value compared to other modified exosomes, though insignificantly (2.11 ± 0.40 x10^{-2} µm^2/s). This reduced average diffusion of mExo-BP can be attributed to its charge distribution. The outermost cationic block on the C-terminus of the peptide can interact with the negatively charged mucin networks. While these interface interactions initially slow the diffusion of mExo-BP by promoting adherence, they are weak and reversible, allowing the majority of mExo-BP particles to eventually mobilize [7].

3.5 Caco-2 cellular uptake, cytotoxicity studies and immunogenicity response

Considerable fluorescence and similar cellular uptake were observed after 2.5 h treatment with native mExo, PEGylated mExo, mExo-DLPC and mExo-MP in Caco-2 cells (**Fig. 4A**). However, mExo surface modified by AP and BP presented 1.5x and 2.5x higher Caco-2 cellular uptake than other groups, respectively (**Fig. 4B**). The MTT assay confirmed the low cytotoxicity of native and surface-modified mExos, as all the Caco-2 groups treated with native and surface-modified mExos showed cellular viabilities higher than 90% (**Fig. 4C**). The surface expression of all pro-inflammatory M1 (CD 86, 197, 80) markers was higher in M1-polarized human monocyte derived macrophages (positive control) than those treated with mExo or mExo-BP, while M2 markers across conditions were similar (**Fig. S4**). Treatment with mExo-BP did not elevate pro-inflammatory markers relative to mExo, suggesting that the zwitterionic BP motif is non-immunogenic.

3.6 Molecular Dynamics (MD) simulation of peptides

To better comprehend the superior stability and cellular uptake properties of mExo-AP and mExo-BP, we carried out molecular dynamics (MD) simulations using Schrödinger. This enabled us to investigate the secondary structure and stability variances between AP and BP peptides in environments with pH 7 and pH 2.2. BP demonstrated superior stability, showing less displacement change across the total peptide and each residue, as indicated by RMSD (**Fig. 5A**) and RMSF (**Fig. S5**). AlphaFold predictions revealed comparable α-helical structures for both AP and BP. However, during MD simulations, BP displayed a higher secondary structure element (% SSE) in both pH 7 (AP: 54.3% vs BP: 72.6%) and pH 2.2 (AP: 33.2% vs BP: 68.7%) environments (**Fig. 5B**). We visualized these changes in

secondary structure during the simulation, revealing that AP tends to form a randomly coiled structure, while BP primarily maintains its α-helical structure (**Fig. 5C, Movies. S1-4**). These observations suggest that the enhanced stability of BP contributes to its superior performance in experimental evaluations.

MP, in both AlphaFold prediction and during MD simulations, did not show any indications of forming secondary structures (**Movies. S5-6)**, underscoring the unique properties of AP and BP.

3.7 siRNA loading and gene silencing

eGFP siRNA was loaded into mExo using the chemical transfection reagent Lipofectamine 2000, as exosomes have a similar membrane structure to cells (**Fig. 6A**). The siRNA loading efficiency was 35.4 ± 0.3%, calculated by dividing the amount of loaded siRNA in mExo by the total amount of siRNA added. 100 µg of mExo had approximately 37.7 pmol of siRNA loaded. We selected GFP-expressing HEK293 cells as a model to evaluate the transfection efficiency of siRNA delivered by native and surface-modified mExos. Non-treated HEK293 and Lipo-siRNA treated HEK293 cells were chosen as negative and positive controls, respectively. A dose dependent GFP silencing efficiency was observed with 5 pmol (62.0 ± 0.1%) and 20 pmol (74.5 ± 1.5%) Lipo-siRNA per well treatment (**Fig. 6B, C**). In contrast, native mExo, mExo-PEG, and mExo-BP showed similar gene silencing efficiency to the Lipo-siRNA complexes when delivering 5 pmol siRNA. However, the gene silencing efficiency did not change at high doses of mExo-delivered siRNA (20 pmol) in all the mExo groups. This result suggests that mExo formulations efficiently deliver siRNA, resulting in cytosolic siRNA concentrations high enough for maximal gene silencing at lower treatment doses compared to Lipofectamine. This finding may be further confounded by the improved tolerability of cells to mExo formulations compared to Lipofectamine, which is well-known for its cytotoxicity at high doses [36].

4. Discussion

In this work, we successfully demonstrated the feasibility of modifying the surface of milk-derived exosomes (mExo) with hydrophilic and zwitterionic motifs for oral delivery of siRNA, with improved stability, accelerated mucus transport and increased cellular uptake. Milk-derived exosomes have gained significant attention in recent years as a promising oral drug delivery system owing to their biocompatibility and non-immunogenicity. In fact, it has been hypothesized that mExos in breast milk aid the transfer of biologically active molecules from mother to child via the oral route, providing nutrition and important growth factors for intestine, immunity, metabolism, and the nervous system [37]. Our earlier work showed a method for harvesting high yield and purity bovine mExo, marking them as viable natural oral delivery nanocarrier [6]. In previous reports, several drugs, including paclitaxel, insulin, and α-mangostin, were loaded in mExo that exhibited improved bioavailability compared to their freely delivered counterparts [38-40]. It is important for mExo as drug carriers to maintain their integrity and reach systemic circulation intact. However, they face two primary challenges via oral administration: degradation in the harsh GI environment and hindered transport while crossing the mucus-epithelial barrier [7]. Our *in vitro* experiments showed that native mExo lost about 85% of proteins in the simulated gastric environment (**Fig. 2D**) and had limited mucus diffusion, with 75% of the population being immobile in FRAP (**Fig. 3D, Movie. S1**). These findings highlight the need for mExo to be engineered in a more stabilized form to enhance oral delivery efficiency.

While many current strategies on exosome engineering focus on enhancing disease targeting, the engineering of mExo for improving oral bioavailability has been understudied. In this study, we successfully harvested high yield mExos from bovine milk and adeptly engineered their surfaces using three distinct strategies (**Figs. 1C, 2C**) [6]. Regarding stability, there was no significant change in size and protein content observed for both native and engineered mExo when exposed to SSF as compared to untreated controls. Notably, mExo-DLPC did not show improved protein recovery as was observed with the other hydrophilic or zwitterionic modified formulations in SGF. Thus, even though mExo-DLPC displayed enhanced diffusivity (**Fig. 4B**), the failure of DLPC to confer stability in simulated gastric conditions suggests that PEGylation is a crucial requirement. As a result, anchoring of AP and BP further protected mExo owing to the combination of PEGylation and the zwitterionic surface [41, 42], which successfully maintained 67.7% and 84.8% protein content, respectively, without exhibiting any aggregation (**Fig. 2D**). Moreover, both AP and BP are rich in alanine, lysine, and glutamic acid, which facilitate the formation of rigid α-helical structures, contributing to their improved stability [43].

We evaluated the functionality of engineered mExo variants using *in vitro* mucus permeability experiments. Using the transwell setup, mExo-AP and mExo-BP displayed superior transport through intestinal mucus compared to native mExos, thus validating our virus-mimicking strategies that incorporate both hydrophilic and zwitterionic modifications to enhance mucus penetration (**Fig. 3B**). In the Fluorescence Recovery After Photobleaching (FRAP) experiments, mExo-AP showed a similar enhancement in diffusivity, demonstrating unimpeded transport akin to mExo-PEG, mExo-MP, and mExo-DLPC (**Fig. 3D**). Interestingly, the relative increase in diffusivity exhibited by mExo-BP compared to control observed in transwell experiments was less prominent when measured by FRAP. This might be attributed to the presence of positive ions on the outermost layer of mExo, which can facilitate electrostatic binding interactions with negatively charged mucin networks at the microscale [7, 44]. The cationic block on mExo-BP can influence mucus transport in multiple ways. Upon first contact between mExo-BP and mucus, the cationic residue blocks allow for immediate Donnan partitioning of mExo-BP at the "luminal" mucus interface, thus setting up a concentration gradient over the mucus layer and enhancing transport [44]. Despite the presence of binding interactions between mExo-BP cationic blocks and the mucin network, this binding is weak and reversible [7], and the driving concentration gradient allows

mExo-BP to penetrate through mucus fast [45]. This weak, reversible binding was evidenced by the FRAP curve of mExo-BP, which showed a slower recovery rate compared to mExo-PEG, but it eventually reached its initial fluorescence, which significantly higher than native mExo (**Fig. S3, Movies. S7-9**). Further probing by modifying the residue number on the cationic block may contribute to optimized structure for more efficient mucus penetration. Consideration of these transport mechanisms is of utmost importance when designing surface modifications for mExo; importantly, if more cationic charge was introduced, these interactions would become too strong and immobilize the mExo within the mucus surface, hence limiting their penetration [7, 23]. Thus, the length, net charge, and spatial placement of any cationic block on the mExo surface must be carefully optimized to avoid making the particle too mucoadhesive, which could limit trans-epithelial transport. In contrast to this strategy, reported mucus-adhesive drug delivery systems make use of strong charge interactions for sustained drug release by implanting cationic carriers in the negatively charged mucus surface [5, 46]. This type of cationic carrier does not penetrate through mucus; rather, the released free drugs can rapidly diffuse into the deep layer of mucus due to the high drug concentration gradient. For instance, chitosan, a mucoadhesive material, provides a cationic surface that allows attachment to negatively charged sialic groups in mucins, enabling modified nanoparticles to sustain drug delivery [46]. These principles of optimal net charge design based on the negative fixed charge density of tissues were confirmed and successfully applied to the development of cartilage targeting carriers in our previous work [47-51].

Remarkably, mExo-AP and mExo-BP demonstrated enhanced uptake in Caco-2 cells compared to other formulations, with improvements of 1.5-fold and 2.5-fold, respectively (**Fig. 4B**). The superior cellular uptake of BP can be attributed to the positively charged block on the outermost layer of the mExo. This facilitates electrostatic interactions with the negatively charged cell membrane, thereby increasing the frequency of mExo-cell contact [23, 52]. Furthermore, current research suggests that a rigid and stable helical structure improves cellular permeability [53]. Hence, the predicted α-helical configurations of both AP and BP in our study may play a critical role in augmenting their uptake by Caco-2 cells.

To further understand the superior cellular uptake and stability of mExo-BP and mExo-AP compared to the other formulations, we conducted MD simulations for both peptides under conditions of pH 7 and pH 2.2. Although AP and BP show similar α-helical structures in the initial AlphaFold predictions, BP exhibited less conformational change and a more stable α-helical element after a 100 ns MD simulation (**Fig. 5A, B, Movie. S1-4**). This may be due to the additional salt bridges (**Fig. 5C, yellow arrow**) between the middle residues in BP. The spatial configuration of glutamic acid and lysine in BP, specifically their placement three residues apart, facilitates electrostatic interactions between their respective cationic and anionic side groups [54]. This interaction contributes to maintaining a stable structural framework [55]. However, AP deviates from an initial alpha helical structure into a folded conformation (**Fig. 5C, red arrow**) between separated residues when fluctuating. Therefore, AP adopted a new structure showing relatively low RMSF (**Fig. S5**), but no longer maintained its original secondary structure (**Fig. 5B**). Additionally, we simulated MP in the same conditions which did not show any tertiary structure formation (**Movies. S5-6**), consistent with the performance of mExo-MP (which did not significantly improve the epithelial uptake (**Fig. 4B**)). Therefore, the relative stability of BP's α-helical structure could contribute to its improved intestinal epithelial permeability. A more stable helical structure could maintain the functional properties of the peptide, allowing it to facilitate the effective transport of mExo across the intestinal epithelial barrier [52, 53]. These findings highlight mExo-BP as an effective oral delivery carrier capable of withstanding the GI environment and facilitating mucus-epithelial transport.

Although the gene silencing potential of small interfering RNA (siRNA) has been harnessed for numerous biomedical applications, its delivery remains a significant challenge due to the steep thermodynamic barrier across cell membranes and susceptibility to RNase degradation during systemic circulation [6, 41]. When using mExo as a siRNA carrier, the high molecular weight of siRNA poses an additional challenge for its loading into mExo without causing disruption to the particle's lipid bilayer. To address this, we previously developed a method to load siRNA into mExo using Lipofectamine-2000 that achieved a loading efficiency of 58%, a performance surpassing techniques such as ExoFect and electroporation [6]. In the current study, to assess the therapeutic delivery efficiency of surface-modified mExos, we implemented the same loading method and subsequently evaluated performance in siRNA-mediated gene silencing via dose-dependent studies. While direct transfection of 20 pmol of siRNA with Lipofectamine demonstrated greater gene silencing than the mExo groups, it is known that higher concentrations of transfection reagents induce increased cytotoxicity [36]. Interestingly, a 5 pmol dose of siRNA, delivered by both native and surface-modified mExo, resulted in gene silencing efficiency comparable to the positive control group (**Fig. 6B, C**). The same transfection efficiency between low and high dosages suggests that both native and surface modified mExo already reached their saturation of transcriptional silencing capability even at this low dose [6]. Meantime, these doses of surface modified mExos did not induce any significant cytotoxicity, even BP had electrostatic interaction with the cells (**Fig. 4C**) [56, 57].

5. Conclusion

In summary, we have demonstrated that surface modification of milk exosomes with hydrophilic and zwitterionic peptides confers particle stability, enhances permeability through intestinal mucus, and improves uptake by intestinal epithelial cells. We utilized a modular, click-chemistry-based post-insertion technique with a high surface loading efficiency, which resulted in favorable neutralization of particle zeta potential without aggregation. The engineered mExo demonstrated markedly increased stability in simulated salivary, gastric, and intestinal fluids compared to native

particles. Further, by shielding the zeta potential of mExo as well as hydrophobic surface properties of the lipid bilayer, mucus binding was reduced, and the zwitterionic-modified particles showed substantially increased mobility in intestinal mucus as measured by bulk transport and FRAP. We observed that the spatial distribution of ionic residues along the surface-loaded peptides is an important design consideration, as the presence of cationic residue blocks (as opposed to alternating zwitterionic charges) influences mucus diffusivity and cell-uptake properties. The mExo-BP variant, which possesses a more stable motif than mExo-AP displayed on the outermost layer, exhibited excellent performance in the functional tests herein: 84.8% protein content recovery in enzyme defected SGF, 2.5-fold epithelial penetration, and improved mucus penetration. These results suggest the significant potential for mExo-BP to serve as a stable oral drug delivery system with high bioactivity. A limitation to this work is that we used simulated GI fluids instead of administering mExos in the *in vivo* GI environment. In future work, enteric coatings on exosome surface should be considered [9]. Moreover, gene silencing potency of modified mExo-delivered siRNA was performed in a GFP-expressing HEK293 cell model only. *In vivo* models will be required to evaluate the biodistribution and bioavailability of engineered mExo containing siRNA following their administration via the oral route.

Conflicts of interest

There are no conflicts to declare.

Acknowledgements

This study was supported by the National Science Foundation (NSF) Career Award 2141841 and by the National Institute of Health (NIH) Trailblazer R21 grant EB028385.

References

1. J. Y. Lock, T. L. Carlson and R. L. Carrier, *Adv Drug Deliv Rev*, 2018, **124**, 34-49.
2. J. S. Crater and R. L. Carrier, *Macromol Biosci*, 2010, **10**, 1473-1483.
3. H. M. Yildiz, C. A. McKelvey, P. J. Marsac and R. L. Carrier, *J Drug Target*, 2015, **23**, 768-774.
4. T. L. Carlson, H. Yildiz, Z. Dar, J. Y. Lock and R. L. Carrier, *PLoS One*, 2018, **13**, e0209151.
5. D. A. Subramanian, R. Langer and G. Traverso, *Journal of Nanobiotechnology*, 2022, **20**, 362.
6. M. R. Warren, C. Zhang, A. Vedadghavami, K. Bokvist, P. K. Dhal and A. G. Bajpayee, *Biomaterials Science*, 2021, **9**, 4260-4277.
7. A. Vedadghavami, C. Zhang and A. G. Bajpayee, *Nano Today*, 2020, **34**, 100898.
8. P. Viswanathan, Y. Muralidaran and G. Ragavan, in *Nanostructures for Oral Medicine*, eds. E. Andronescu and A. M. Grumezescu, Elsevier, 2017, DOI: https://doi.org/10.1016/B978-0-323-47720-8.00008-0, pp. 173-201.
9. A. R. Kirtane, T. Hua, A. Hayward, A. Bajpayee, A. Wahane, A. Lopes, T. Bensel, L. Ma, F. Z. Stanczyk, S. Brooks, D. Gwynne, J. Wainer, J. Collins, S. M. Tamang, R. Langer and G. Traverso, *Science Translational Medicine*, 2019, **11**, eaay2602.
10. A. Hayward, T. Bensel, H. Mazdiyasni, J. Rogner, A. R. Kirtane, Y. L. Lee, T. Hua, A. Bajpayee, J. Collins, S. McDonnell, C. Cleveland, A. Lopes, A. Wahane, R. Langer and G. Traverso, *Sci Rep*, 2018, **8**, 11816.
11. S. Fu, Y. Wang, X. Xia and J. C. Zheng, *NanoImpact*, 2020, **20**, 100261.
12. X. Luan, K. Sansanaphongpricha, I. Myers, H. Chen, H. Yuan and D. Sun, *Acta Pharmacologica Sinica*, 2017, **38**, 754-763.
13. Y. Y. Wang, S. K. Lai, J. S. Suk, A. Pace, R. Cone and J. Hanes, *Angew Chem Int Ed Engl*, 2008, **47**, 9726-9729.
14. A. Cobarrubia, J. Tall, A. Crispin-Smith and A. Luque, *Frontiers in Physics*, 2021, **9**.
15. J. L. Betker, B. M. Angle, M. W. Graner and T. J. Anchordoquy, *J Pharm Sci*, 2019, **108**, 1496-1505.
16. T. Wolf, S. R. Baier and J. Zempleni, *J Nutr*, 2015, **145**, 2201-2206.
17. R. J. Kusuma, S. Manca, T. Friemel, S. Sukreet, C. Nguyen and J. Zempleni, *Am J Physiol Cell Physiol*, 2016, **310**, C800-807.
18. M. Somiya, Y. Yoshioka and T. Ochiya, *J Extracell Vesicles*, 2018, **7**, 1440132.
19. J. Leal, T. Dong, A. Taylor, E. Siegrist, F. Gao, H. D. C. Smyth and D. Ghosh, *Int J Pharm*, 2018, **553**, 57-64.
20. J. Li, H. Qiang, W. Yang, Y. Xu, T. Feng, H. Cai, S. Wang, Z. Liu, Z. Zhang and J. Zhang, *Journal of Controlled Release*, 2022, **341**, 31-43.
21. S. Hu, Z. Yang, S. Wang, L. Wang, Q. He, H. Tang, P. Ji and T. Chen, *Chemical Engineering Journal*, 2022, **428**, 132107.
22. W. Shan, X. Zhu, W. Tao, Y. Cui, M. Liu, L. Wu, L. Li, Y. Zheng and Y. Huang, *ACS Applied Materials & Interfaces*, 2016, **8**, 25444-25453.
23. Leon D. Li, T. Crouzier, A. Sarkar, L. Dunphy, J. Han and K. Ribbeck, *Biophysical Journal*, 2013, **105**, 1357-1365.
24. M. Minekus, M. Alminger, P. Alvito, S. Ballance, T. Bohn, C. Bourlieu, F. Carrière, R. Boutrou, M. Corredig, D. Dupont, C. Dufour, L. Egger, M. Golding, S. Karakaya, B. Kirkhus, S. Le Feunteun, U. Lesmes, A. Macierzanka, A. Mackie, S. Marze, D. J. McClements, O. Ménard, I. Recio, C. N. Santos, R. P. Singh, G. E. Vegarud, M. S. J. Wickham, W. Weitschies and A. Brodkorb, *Food & Function*, 2014, **5**, 1113-1124.
25. O. Rezhdo, S. Di Maio, P. Le, K. C. Littrell, R. L. Carrier and S. H. Chen, *J Colloid Interface Sci*, 2017, **499**, 189-201.
26. D. Axelrod, D. E. Koppel, J. Schlessinger, E. Elson and W. W. Webb, *Biophysical Journal*, 1976, **16**, 1055-1069.
27. T. K. L. Meyvis, S. C. De Smedt, P. Van Oostveldt and J. Demeester, *Pharmaceutical Research*, 1999, **16**, 1153-1162.
28. A. Mily, S. Kalsum, M. G. Loreti, R. S. Rekha, J. R. Muvva, M. Lourda and S. Brighenti, *J Vis Exp*, 2020, DOI: 10.3791/61807.
29. J. Rao Muvva, V. R. Parasa, M. Lerm, M. Svensson and S. Brighenti, *Front Immunol*, 2019, **10**, 3157.
30. Y. Zhou, S. Yoshida, Y. Kubo, T. Yoshimura, Y. Kobayashi, T. Nakama, M. Yamaguchi, K. Ishikawa, Y. Oshima and T. Ishibashi, *Mol Med Rep*, 2017, **15**, 3949-3956.

31. J. Jumper, R. Evans, A. Pritzel, T. Green, M. Figurnov, O. Ronneberger, K. Tunyasuvunakool, R. Bates, A. Žídek, A. Potapenko, A. Bridgland, C. Meyer, S. A. A. Kohl, A. J. Ballard, A. Cowie, B. Romera-Paredes, S. Nikolov, R. Jain, J. Adler, T. Back, S. Petersen, D. Reiman, E. Clancy, M. Zielinski, M. Steinegger, M. Pacholska, T. Berghammer, S. Bodenstein, D. Silver, O. Vinyals, A. W. Senior, K. Kavukcuoglu, P. Kohli and D. Hassabis, *Nature*, 2021, **596**, 583-589.
32. M. Varadi, S. Anyango, M. Deshpande, S. Nair, C. Natassia, G. Yordanova, D. Yuan, O. Stroe, G. Wood, A. Laydon, A. Žídek, T. Green, K. Tunyasuvunakool, S. Petersen, J. Jumper, E. Clancy, R. Green, A. Vora, M. Lutfi, M. Figurnov, A. Cowie, N. Hobbs, P. Kohli, G. Kleywegt, E. Birney, D. Hassabis and S. Velankar, *Nucleic Acids Research*, 2022, **50**, D439-D444.
33. C. Lu, C. Wu, D. Ghoreishi, W. Chen, L. Wang, W. Damm, G. A. Ross, M. K. Dahlgren, E. Russell, C. D. Von Bargen, R. Abel, R. A. Friesner and E. D. Harder, *Journal of Chemical Theory and Computation*, 2021, **17**, 4291-4300.
34. G. J. Martyna, D. J. Tobias and M. L. Klein, *The Journal of Chemical Physics*, 1994, **101**, 4177-4189.
35. W. G. Hoover, *Physical Review A*, 1985, **31**, 1695-1697.
36. T. Wang, L. M. Larcher, L. Ma and R. N. Veedu, *Molecules*, 2018, **23**.
37. Y. Zheng, S. Correa-Silva, P. Palmeira and M. Carneiro-Sampaio, *Clinics (Sao Paulo)*, 2022, **77**, 100093.
38. A. K. Agrawal, F. Aqil, J. Jeyabalan, W. A. Spencer, J. Beck, B. W. Gachuki, S. S. Alhakeem, K. Oben, R. Munagala, S. Bondada and R. C. Gupta, *Nanomedicine: Nanotechnology, Biology and Medicine*, 2017, **13**, 1627-1636.
39. L. Wu, L. Wang, X. Liu, Y. Bai, R. Wu, X. Li, Y. Mao, L. Zhang, Y. Zheng, T. Gong, Z. Zhang and Y. Huang, *Acta Pharm Sin B*, 2022, **12**, 2029-2042.
40. S. Qu, Y. Han, Y. Liu, J. Zhu, U. Acaroz, J. Shen and K. Zhu, *Journal of Agricultural and Food Chemistry*, 2022, **70**, 16069-16079.
41. Y. Guo, Y. Ma, X. Chen, M. Li, X. Ma, G. Cheng, C. Xue, Y. Y. Zuo and B. Sun, *ACS Nano*, 2023, **17**, 2813-2828.
42. R. Rajan and K. Matsumura, *Scientific Reports*, 2017, **7**, 45777.
43. X. Chen, J. L. Zaro and W.-C. Shen, *Advanced Drug Delivery Reviews*, 2013, **65**, 1357-1369.
44. A. G. Bajpayee and A. J. Grodzinsky, *Nature Reviews Rheumatology*, 2017, **13**, 183-193.
45. C. C. Young, A. Vedadghavami and A. G. Bajpayee, *Bioelectricity*, 2020, **2**, 68-81.
46. I. Bravo-Osuna, C. Vauthier, A. Farabollini, G. F. Palmieri and G. Ponchel, *Biomaterials*, 2007, **28**, 2233-2243.
47. A. Vedadghavami, E. K. Wagner, S. Mehta, T. He, C. Zhang and A. G. Bajpayee, *Acta Biomaterialia*, 2019, **93**, 258-269.
48. T. He, C. Zhang, A. Vedadghavami, S. Mehta, H. A. Clark, R. M. Porter and A. G. Bajpayee, *J Control Release*, 2020, **318**, 109-123.
49. S. Mehta, T. L. Boyer, S. Akhtar, T. He, C. Zhang, A. Vedadghavami and A. G. Bajpayee, *Osteoarthritis and Cartilage*, 2023, **31**, 780-792.
50. A. Vedadghavami, T. He, C. Zhang, S. M. Amiji, B. Hakim and A. G. Bajpayee, *Acta Biomaterialia*, 2022, **151**, 278-289.
51. C. Zhang, A. Vedadghavami, T. He, J. F. Charles and A. G. Bajpayee, *ACS Nano*, 2023, **17**, 6649-6663.
52. E. Eiríksdóttir, K. Konate, Ü. Langel, G. Divita and S. Deshayes, *Biochimica et Biophysica Acta (BBA) - Biomembranes*, 2010, **1798**, 1119-1128.
53. G. Lättig-Tünnemann, M. Prinz, D. Hoffmann, J. Behlke, C. Palm-Apergi, I. Morano, H. D. Herce and M. C. Cardoso, *Nature Communications*, 2011, **2**, 453.
54. P. Morales and M. A. Jiménez, *Archives of Biochemistry and Biophysics*, 2019, **661**, 149-167.
55. A. L. Boyle, in *Peptide Applications in Biomedicine, Biotechnology and Bioengineering*, ed. S. Koutsopoulos, Woodhead Publishing, 2018, DOI: https://doi.org/10.1016/B978-0-08-100736-5.00003-X, pp. 51-86.
56. M. R. Warren and A. G. Bajpayee, *Bioelectricity*, 2022, **4**, 248-258.
57. M. R. Warren, A. Vedadghavami, S. Bhagavatula and A. G. Bajpayee, *Biophys J*, 2022, **121**, 3542-3561.

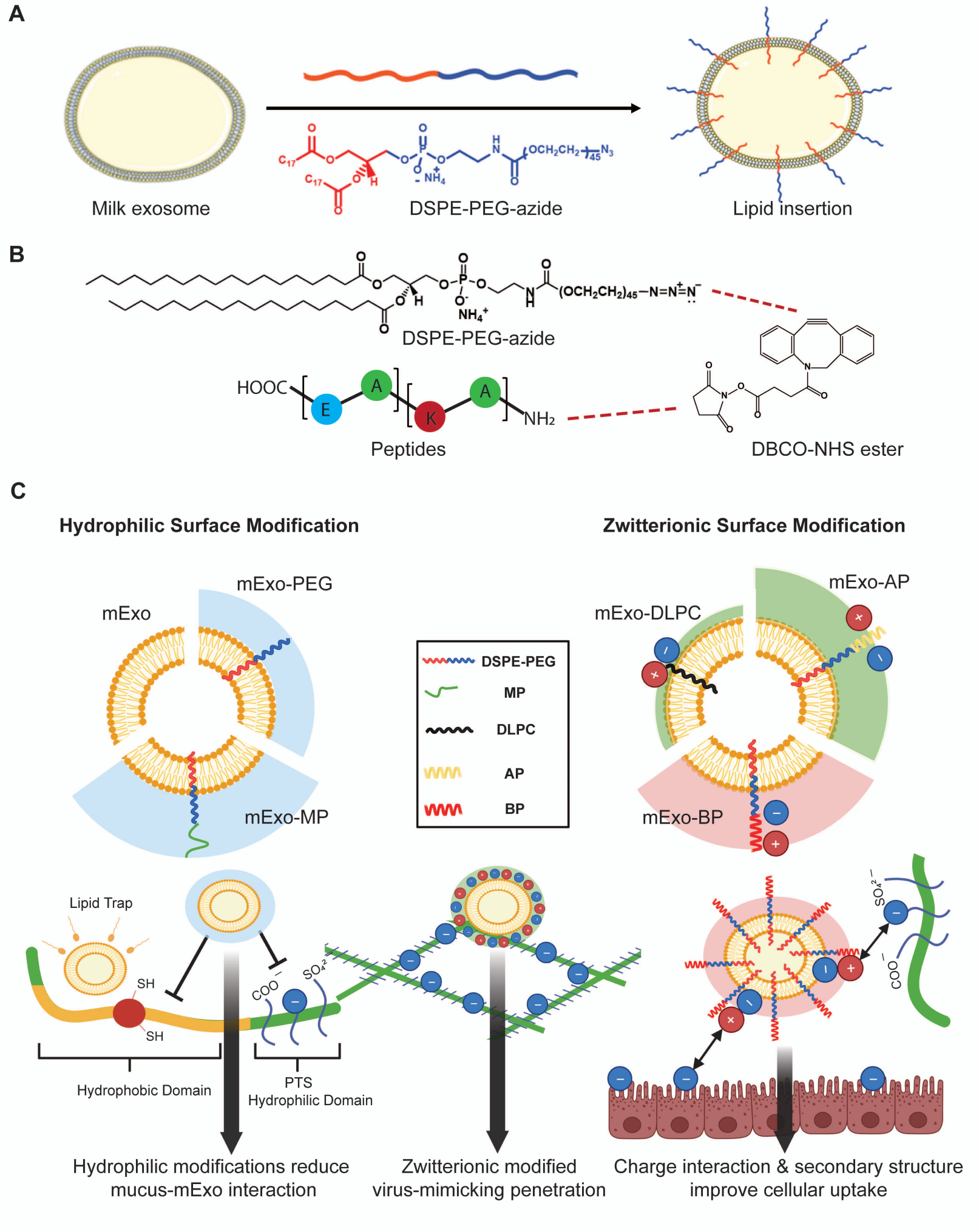
A
Milk exosome
DSPE-PEG-azide
Lipid insertion
B
DSPE-PEG-azide
HOOC
E
A
K
A
NH2
Peptides
DBCO-NHS ester
C
Hydrophilic Surface Modification
Zwitterionic Surface Modification
mExo
mExo-PEG
mExo-MP
DSPE-PEG
MP
DLPC
AP
BP
mExo-DLPC
mExo-AP
mExo-BP
Lipid Trap
SH
SH
COO⁻
SO4 2-
Hydrophobic Domain
PTS
Hydrophilic Domain
Hydrophilic modifications reduce mucus-mExo interaction
Zwitterionic modified virus-mimicking penetration
Charge interaction & secondary structure improve cellular uptake

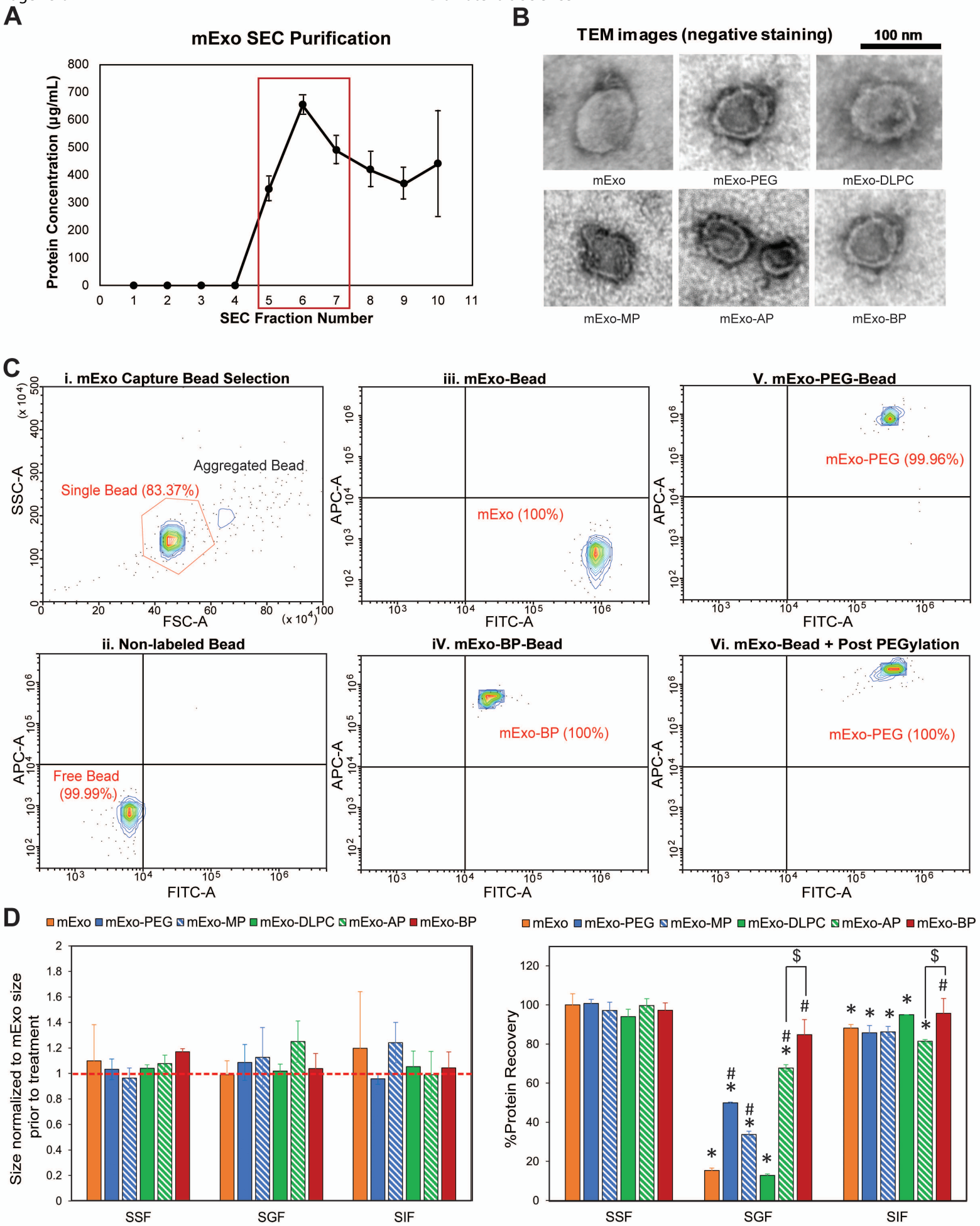
A
mExo SEC Purification
Protein Concentration (μg/mL)
SEC Fraction Number
B
TEM images (negative staining)
100 nm
mExo
mExo-PEG
mExo-DLPC
mExo-MP
mExo-AP
mExo-BP
C
i. mExo Capture Bead Selection
Single Bead (83.37%)
Aggregated Bead
SSC-A
FSC-A
iii. mExo-Bead
mExo (100%)
V. mExo-PEG-Bead
mExo-PEG (99.96%)
ii. Non-labeled Bead
Free Bead (99.99%)
iV. mExo-BP-Bead
mExo-BP (100%)
Vi. mExo-Bead + Post PEGylation
mExo-PEG (100%)
APC-A
FITC-A
D
mExo mExo-PEG mExo-MP mExo-DLPC mExo-AP mExo-BP
Size normalized to mExo size prior to treatment
%Protein Recovery
SSF
SGF
SIF

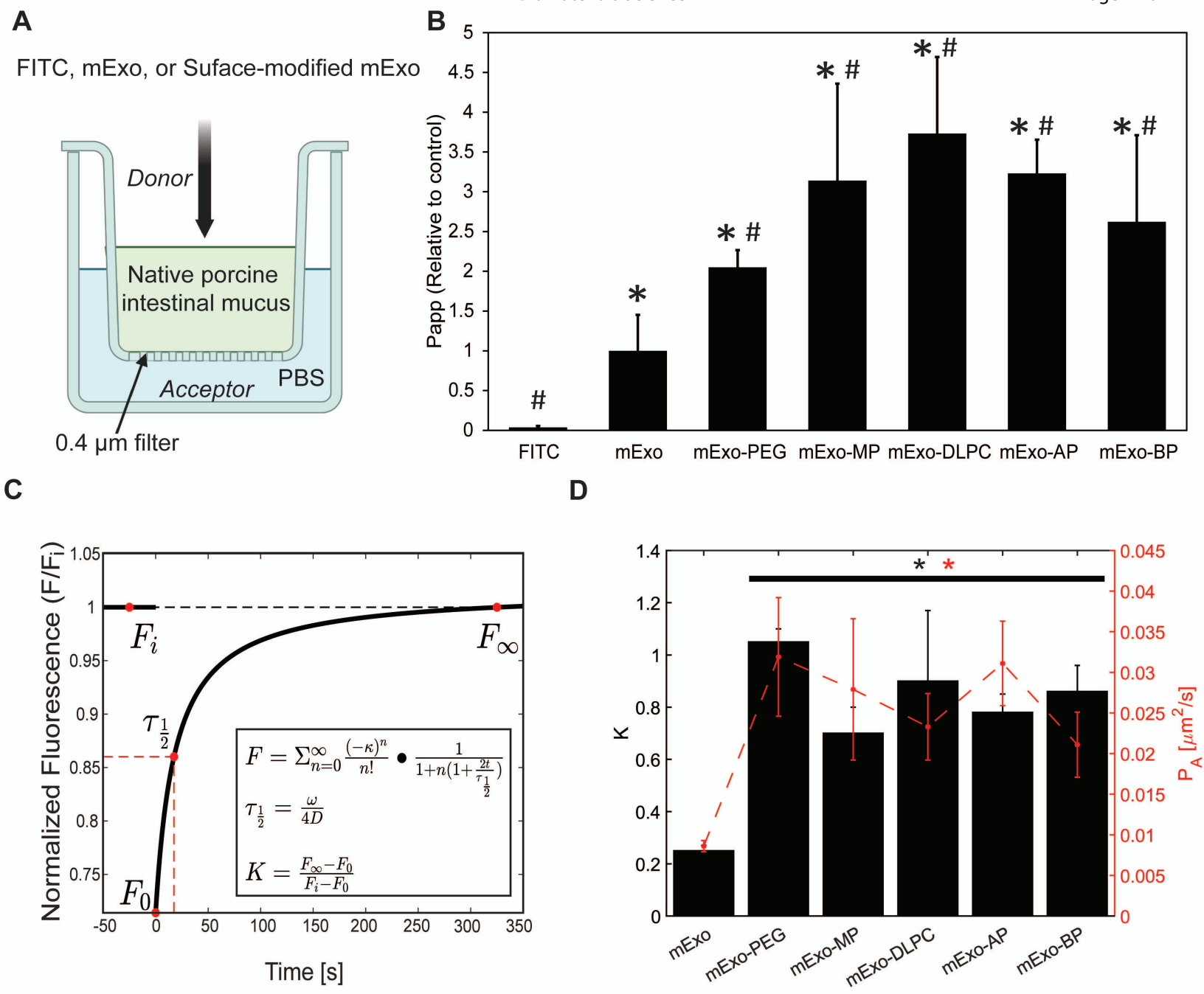
A
FITC, mExo, or Suface-modified mExo
Donor
Native porcine intestinal mucus
Acceptor
PBS
0.4 μm filter
B
Papp (Relative to control)
FITC
mExo
mExo-PEG
mExo-MP
mExo-DLPC
mExo-AP
mExo-BP
C
Normalized Fluorescence (F/Fi)
Time [s]
$F = \Sigma_{n=0}^{\infty} \frac{(-\kappa)^n}{n!} \bullet \frac{1}{1+n(1+\frac{2t}{\tau_{\frac{1}{2}}})}$
$\tau_{\frac{1}{2}} = \frac{\omega}{4D}$
$K = \frac{F_\infty - F_0}{F_i - F_0}$
D
K
P_A [$\mu m^2/s$]
mExo
mExo-PEG
mExo-MP
mExo-DLPC
mExo-AP
mExo-BP

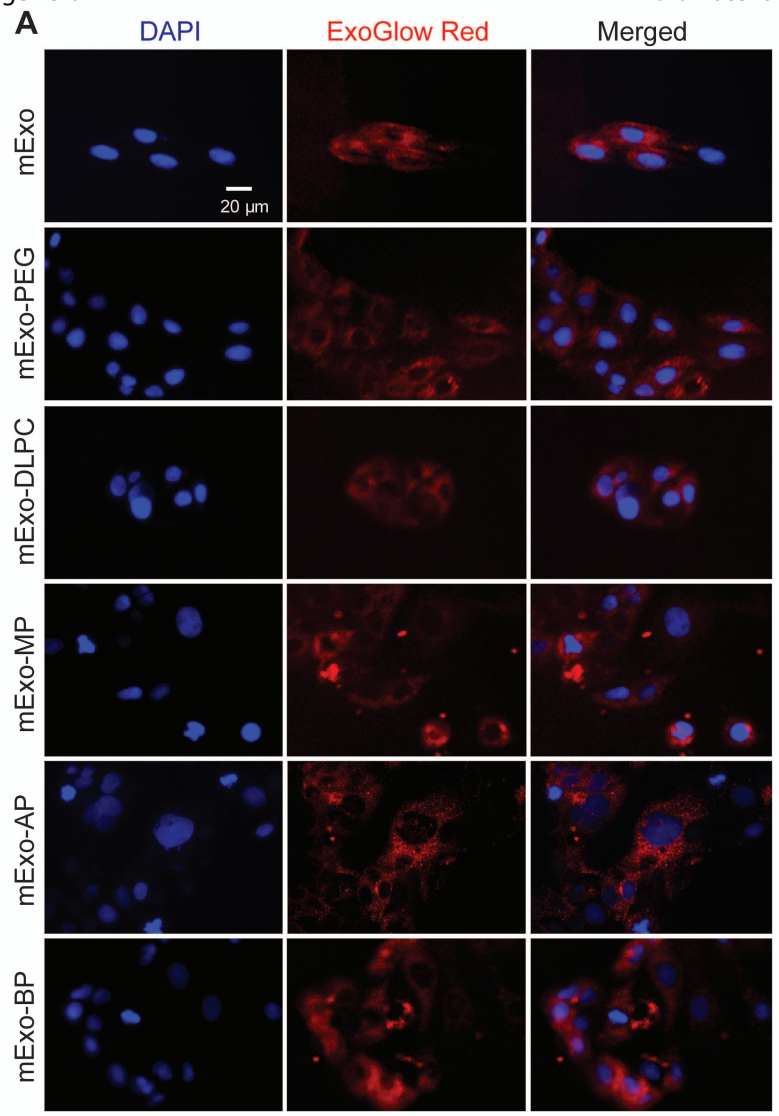
A
DAPI
ExoGlow Red
Merged
mExo
mExo-PEG
mExo-DLPC
mExo-MP
mExo-AP
mExo-BP
20 μm

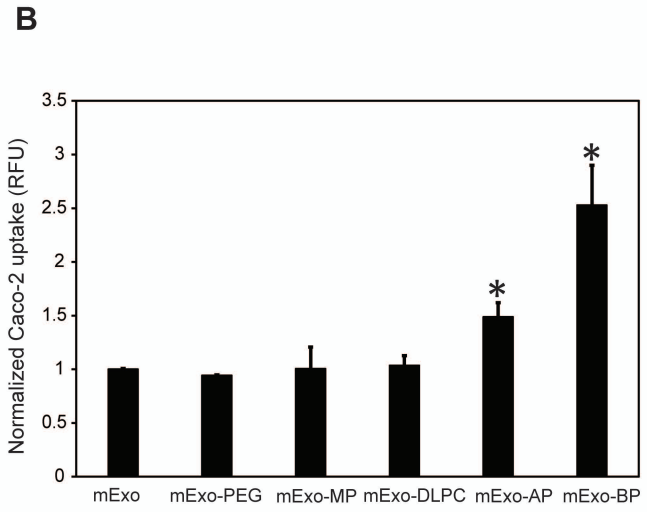
B
Normalized Caco-2 uptake (RFU)
3.5
3
2.5
2
1.5
1
0.5
0
*
*
mExo
mExo-PEG
mExo-MP
mExo-DLPC
mExo-AP
mExo-BP

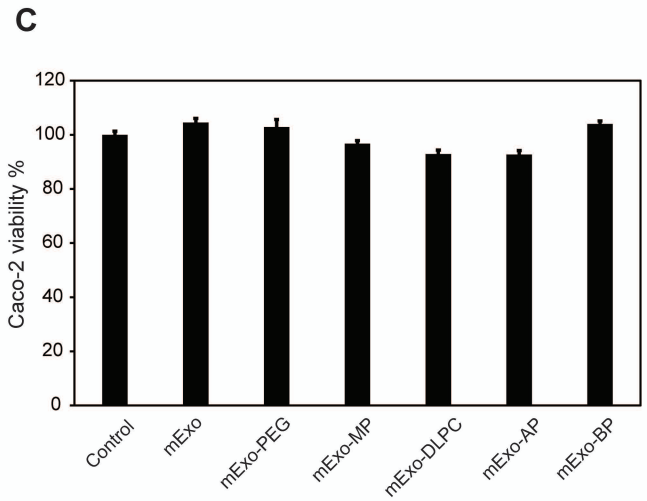
C
Caco-2 viability %
120
100
80
60
40
20
0
Control
mExo
mExo-PEG
mExo-MP
mExo-DLPC
mExo-AP
mExo-BP

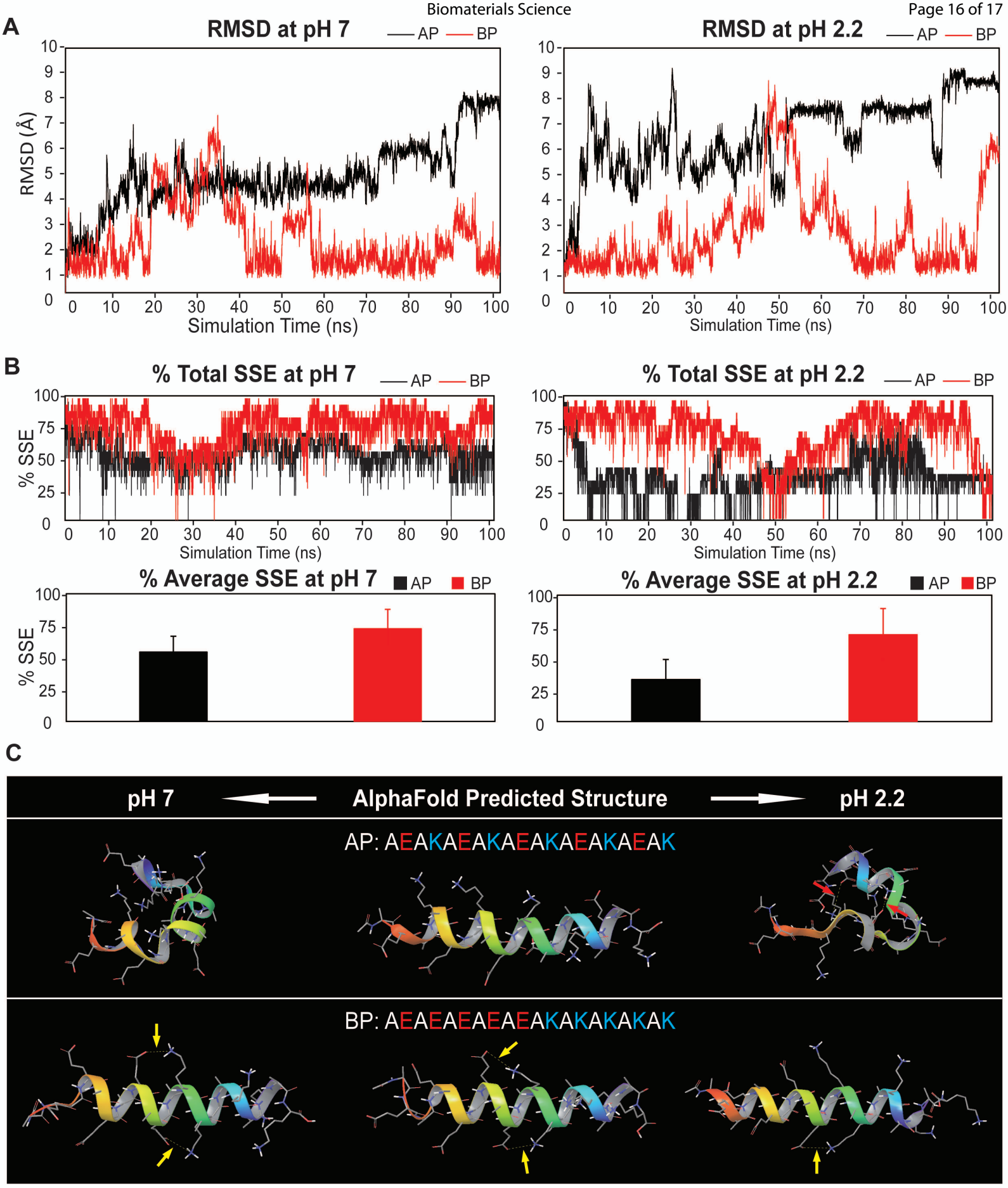
A
RMSD at pH 7
AP
BP
RMSD (Å)
Simulation Time (ns)
RMSD at pH 2.2
AP
BP
Simulation Time (ns)
B
% Total SSE at pH 7
AP
BP
% SSE
Simulation Time (ns)
% Total SSE at pH 2.2
AP
BP
Simulation Time (ns)
% Average SSE at pH 7
AP
BP
% SSE
% Average SSE at pH 2.2
AP
BP
C
pH 7
AlphaFold Predicted Structure
pH 2.2
AP: AEAKAEAKAEAKAEAKAEAK
BP: AEAEAEAEAEAKAKAKAKAK

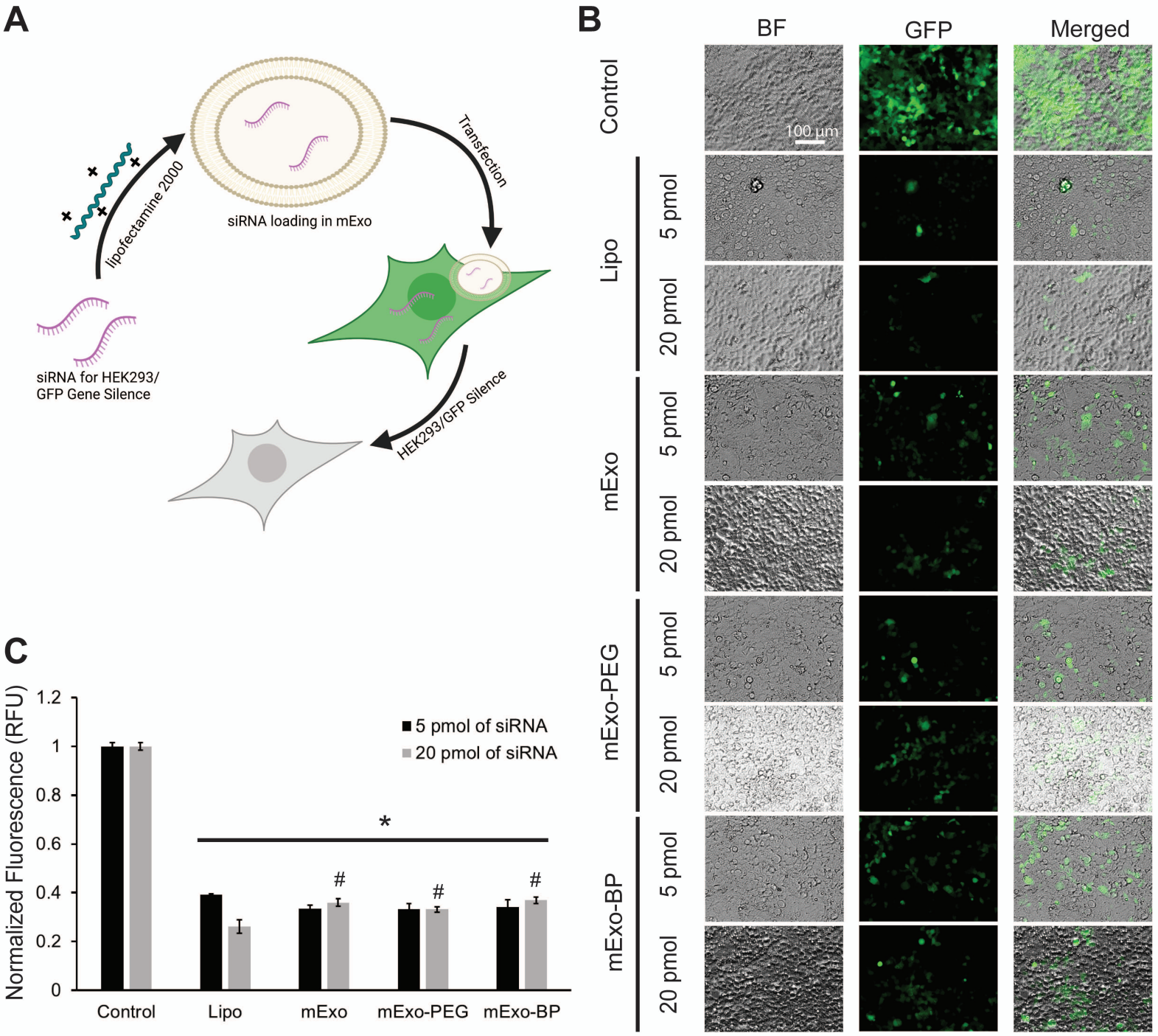
A
siRNA loading in mExo
Transfection
lipofectamine 2000
siRNA for HEK293/
GFP Gene Silence
HEK293/GFP Silence
B
BF
GFP
Merged
Control
Lipo
mExo
mExo-PEG
mExo-BP
5 pmol
20 pmol
100 μm
C
Normalized Fluorescence (RFU)
1.2
1
0.8
0.6
0.4
0.2
0
5 pmol of siRNA
20 pmol of siRNA
*
#
Control
Lipo
mExo
mExo-PEG
mExo-BP